

INVERSE SCATTERING OF THREE-DIMENSIONAL PEC OBJECTS USING THE LEVEL-SET METHOD

M. R. Hajihashemi and M. El-Shenawee

University of Arkansas
Fayetteville, USA

Abstract—A 3D shape reconstruction algorithm for multiple PEC objects immersed in air is presented. The Hamilton-Jacobi PDE is solved in the entire computational domain with employing the marching cubes method to retrieve the unknown objects. The method of moment surface integral equation is used as the forward solver. An appropriate form of the deformation velocity, based on the forward and *adjoint* fields, is implemented to minimize the mismatch between the measurements and simulated scattered fields from the evolving objects. The inversion algorithm demonstrated good shape reconstruction results even when using limited view data or noisy corrupted data with SNR of 5 dB.

1. INTRODUCTION

The shape reconstruction of unknown objects is one of the basic classes of the general inverse scattering techniques. To reduce the degree of the non-linearity of the problem, the constitutive parameters of the target objects are assumed to be *a priori* known in this work. The inversion algorithm tries to find the number of the unknown target objects, their shapes and locations. This information can be retrieved by considering the way that electromagnetic waves are scattered from the unknown objects. This subject is of interest in a variety of applications including nondestructive testing, remote sensing, biomedical applications, medical imaging, and defects detection [1–24]. In this section, we are summarizing several published work related to the inverse scattering of two- and three-dimensional targets, the adjoint fields technique, limitations of related methods, etc.

For example, an iterative three-dimensional (3D) algorithm was applied for detecting breast tumors upon using time-domain microwave data [1]; a nonlinear multisource strategy was presented for the quantitative imaging of two-dimensional (2D) scatterers [2]; and a 2D sliced tomographic reconstruction algorithm was used for imaging 3D strong scatterers validated using experimental data [3].

Shape reconstruction algorithms can be combined with other inverse scattering and stochastic techniques for retrieving both the dielectric properties and the shape of the scattering objects [13, 14]. The linear sampling method was employed for characterizing the support of the targets, followed by using the optimized contrast source extended Born inversion for quantitative characterization of the targets [14]. In the case of perfectly electric conducting (PEC) targets, the inverse scattering problem can be casted as a shape reconstruction problem. Several papers in the literature presented 3D shape reconstructions of dielectric and conducting objects [6, 15–24]. The shape reconstruction of a 3D PEC object using a boundary integral formulation was presented in [15].

The linear sampling is a well-known qualitative technique for reconstructing the shape of scattering objects upon solving a linear integral equation of the first kind; however large amounts of data were required for its successful implementation [13, 14]. The linear sampling method was improved in [16] to reconstruct the shape of 3D targets embedded in a non-accessible region. The algorithm presented in [16] reduced the inherent complexity of the measurement setup and improved the reconstruction of buried targets.

The distorted Born iterative method (DBIM) and the stabilized biconjugate-gradient fast Fourier Transform (BCGS-FFT) were employed for retrieving the profile of 3D dielectric objects using experimental measurement data [17]. The Direct Fourier Interpolation (DFI) and the Filtered Backpropagation (FBP) algorithms were extended in [18] for pixel by pixel reconstruction of the dielectric properties. As known, these methods are restricted to weak scattering objects.

The reconstruction of 3D complex permittivity using the combination of a modified Gauss-Newton method and an efficient forward solver based on the fast Fourier transform method was presented in [19]. The shape reconstruction of simple conducting patches was demonstrated upon applying the Non Uniform Rational Basis Spline (NURBS) geometric modeling and a genetic algorithm [20]. The work in [21] presented a technique for shape reconstruction of 3D perfect electric conducting (PEC) objects upon adopting a distributional formulation for the unknowns of the problem.

Experimental data were used for 3D reconstruction in Electric Capacitance Tomography (ECT) [22]. The finite element was used as the forward solver on a 32 electrode ECT system. A two step approach for reconstruction the shape of 2D PEC objects using a single view and single frequency data was presented in [23].

Note that our previous work in [6] was for reconstructing the shape of 3D dielectric objects with lossy electrical properties to simulate malignant tumors immersed in fatty breast tissue. That work was a parameter based technique that employed the spherical harmonics coefficients as the unknown shape parameters. A brute force calculation of the gradient was implemented using the finite difference scheme with respect to each spherical harmonic coefficient [6]. For better capturing of the irregular tumor shape, the order of the spherical harmonic expansion was increased leading to an increase in the computational time. The current work is not a parameter based optimization, as was the case in [6], but it is an implicit shape reconstruction method based on the level set technique that solves the Hamilton Jacobi equation with respect to the space and time [25–27].

The adjoint field technique is also implemented here for calculating the deformation velocity needed in the level set algorithm. In our work in [24], the shape reconstruction of 3D lossy objects immersed in lossy medium was presented based on updating the re-location of each surface node. The adjoint scheme was employed to calculate the steepest descent gradient direction which was required for the updating process. As known, the advantage of using the adjoint field technique is reducing the computations using the forward solver. The forward solver is called only two times per each frequency and source, compared with the brute force calculation of the gradient with respect to each shape parameter in [6]. However, in [24] the number of unknown objects was needed to be known *a priori*, which was a limitation compared with the current work using the level set technique.

The main contribution of the current work is the implementation of the robust shape reconstruction level set technique for 3D PEC objects. The previous work in [6] and [24] handled single 3D dielectric objects; however, the current work simultaneously handles multiple 3D PEC objects with *no a priori* information about their numbers or shapes. The authors also reported results using the level set technique when the *TE* versus the *TM* polarization was employed in the measurements [28].

The objective of the current work is to reconstruct the shape of multiple 3D perfectly conducting objects using the level set method. Plane waves are employed for illuminating the unknown objects with collecting the scattered fields in the far zone. The measurements data

are synthetic in this work. The electric field surface integral equation (EFIE) is solved using the Method of Moments (MoM) based on Rao-Wilton-Glisson (*RWG*) basis functions [29–32].

2. FORMULATION

In the level set framework, the moving surface is implicitly represented as the zero level of a three-dimensional function $\Phi(\cdot)$. At each time t , the interface $\Gamma(\cdot)$ is expressed as [33, 34]:

$$\Gamma(t) = \{(x, y, z) | \Phi(x, y, z, t) = 0\} \quad (1)$$

Calculating the derivative of (1) with respect to the evolving time leads to the following PDE known as the Hamilton-Jacobi Equation [33]:

$$\frac{\partial}{\partial t} \Phi(x, y, z, t) + F(\bar{r}) \|\nabla \Phi(x, y, z, t)\| = 0 \quad (2a)$$

$$\Phi_0 = \Phi(x, y, z, t = 0) \quad (2b)$$

where $F(\cdot)$ is an appropriate form of the deformation velocity pointing in the normal direction to the evolving surfaces and $r = (x, y, z)$ is the position vector at any point in the computational domain. The symbol $\Phi(\cdot)$ represents the level set function with Φ_0 denotes the initial level set function. The PDE in (2) is solved numerically using the higher order finite difference schemes elaborated in [33].

2.1. Initialization of the Level Set Function Φ_0

The level set function Φ_0 in (2b) is initialized to the signed distance function corresponding to the arbitrary initial guess of the unknown objects. The signed distance function at any point in the computational domain is defined as the distance to the closest point on the surface. If that point is outside the surface, then the signed function is positive otherwise, it is negative [34]. The signed distance function offers the advantage of avoiding steep gradients and/or rapidly changing shape features [34]. If the initial guess is chosen to be a sphere with radius of r_c centered at (x_c, y_c, z_c) , the initialization process for any pixel (x_i, y_j, z_k) in the computational grid is straightforward given by:

$$\Phi_0(x_i, y_j, z_k) = \sqrt{(x_i - x_c)^2 + (y_j - y_c)^2 + (z_k - z_c)^2} - r_c \quad (3)$$

Since we have employed the full-band level set scheme, the level set function is not required to be reinitialized to the signed distance function, during the inversion algorithm.

2.2. Deformation Velocity $F(\cdot)$

In order to solve the inverse scattering problem, a non-linear optimization approach is used to update the surface of the evolving objects. The goal of the algorithm is to minimize the cost function in (4), i.e., the mismatch between the measurements fields and the simulated scattered fields from the evolving objects. The normalized cost function is defined as:

$$\begin{aligned} & \text{Normalized Cost} \\ & \frac{\sum_{i=1}^{N^{inc}} \sum_{m=1}^{N^{meas}} \left\| \bar{P}^{sc}(\theta_i^{inc}, \phi_i^{inc}, \theta_{i,m}^{sc}, \phi_{i,m}^{sc}) - \bar{P}_{meas}^{sc}(\theta_i^{inc}, \phi_i^{inc}, \theta_{i,m}^{sc}, \phi_{i,m}^{sc}) \right\|^2}{\sum_{i=1}^{N^{inc}} \sum_{m=1}^{N^{meas}} \left\| \bar{P}_{meas}^{sc}(\theta_i^{inc}, \phi_i^{inc}, \theta_{i,m}^{sc}, \phi_{i,m}^{sc}) \right\|^2} \end{aligned} \quad (4)$$

The symbol N^{inc} represents the number of incident waves, N_i^{meas} is the number of measurements for the i th incidence $(\theta_i^{inc}, \phi_i^{inc})$ direction, and $(\theta_{i,m}^{meas}, \phi_{i,m}^{meas})$ is the m th scattering direction due to the i th incident plane wave, using the standard spherical coordinate system. The scattered electric field patterns $\bar{P}^{sc}(\cdot)$ are defined as [32]:

$$\bar{P}^{sc}(\theta_i^{inc}, \phi_i^{inc}, \theta_{i,m}^{sc}, \phi_{i,m}^{sc}) = r_o e^{jkr_o} \bar{E}^{sc}(\theta_i^{inc}, \phi_i^{inc}, \theta_{i,m}^{sc}, \phi_{i,m}^{sc}) \quad (5)$$

where $\bar{E}^{sc}(\cdot)$ represents the scattered electric field and $\bar{P}^{sc}(\cdot)$ represents the scattering far field pattern. The distance r_o is chosen to be 50λ which is adequately far from the targets and k is the wave number. For no particular reason, the field pattern is used here instead of the electric field. To achieve convergence, the cost function $Cost$ should be decreasing with respect to the evolving time as follows:

$$\begin{aligned} \frac{dCost}{dt} = 2\text{Re} \left\{ \sum_{i=1}^{N^{inc}} \sum_{m=1}^{N_i^{meas}} \left(\bar{P}^{sc}(\theta_i^{inc}, \phi_i^{inc}, \theta_{i,m}^{sc}, \phi_{i,m}^{sc}) \right. \right. \\ \left. \left. - \bar{P}_{meas}^{sc}(\theta_i^{inc}, \phi_i^{inc}, \theta_{i,m}^{sc}, \phi_{i,m}^{sc}) \right)^* \right. \\ \left. \cdot \frac{d}{dt} \bar{P}^{sc}(\theta_i^{inc}, \phi_i^{inc}, \theta_{i,m}^{sc}, \phi_{i,m}^{sc}) \right\} < 0 \end{aligned} \quad (6)$$

The asterisk in (6) denotes the complex conjugate, $\bar{P}^{sc}(\cdot)$ represents the simulated field pattern and $\bar{P}_{meas}^{sc}(\cdot)$ represents the corresponding measurement of the field pattern. The functional derivative of the electric field pattern with respect to the evolution time t relates the variation rate of the electric far-field pattern due to a small variation of the object's surface. Using the reciprocity theorem leads to the

following expression for the functional derivative of the electric field pattern [35]:

$$\begin{aligned}
& \frac{d}{dt} (\hat{e}' \cdot \bar{P}^{sc}(\theta_i^{inc}, \phi_i^{inc}, \theta_{i,m}^{sc}, \phi_{i,m}^{sc})) \\
&= \frac{-j\omega\mu_0}{8\pi} \int_{S^+} \nabla^+ \cdot (\bar{H} \times \bar{E}') F(\bar{r}) ds \\
&= \frac{-j\omega\mu_0}{8\pi} \int_{S^+} \nabla^+ \cdot (\bar{H}' \times \bar{E}) F(\bar{r}) ds \tag{7}
\end{aligned}$$

The unit vector \hat{e}' specifies the polarization of the plane wave corresponding to the *adjoint* problem; see the schematic description of the adjoint field problem in Figure 1(a). The plus superscript in (7) means that the considered quantity is replaced by its limit approaching the PEC surface from the outside. The fields \bar{E} and \bar{H} in (7) represent the electric and magnetic fields, on the surface of the evolving objects, corresponding to the forward scattering problem, respectively, while the fields \bar{E}' and \bar{H}' represent the fields of the *adjoint* problem. As known, the *adjoint* fields are the solution of the scattering problem when a plane wave illuminates the objects in the direction of $(\theta_{i,m}^{sc} + \pi, \phi_{i,m}^{sc})$. For consistency, the amplitudes and the polarization of the *adjoint* incident waves are determined by the vector

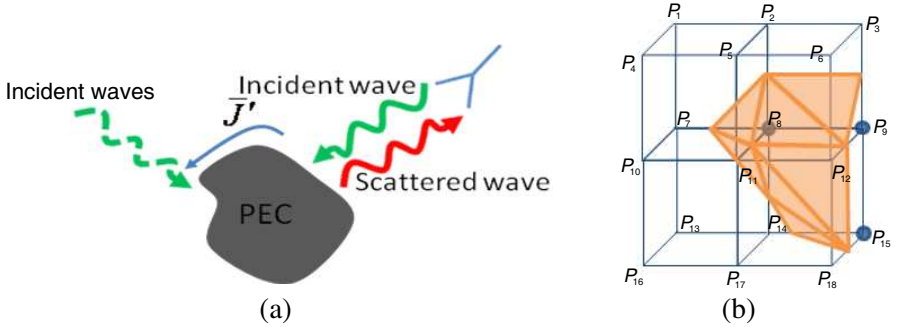


Figure 1. (a) Schematic of the *adjoint* field problem where the target is illuminated using the back propagation waves. The amplitude of this excitation is equal to the complex conjugate of the difference between the scattered fields and the measured fields at the receiver. As a result, the electric surface current density \bar{J}' is excited on the surface of the PEC object. (b) Marching cubes algorithm using four cubes (as an example).

$$(\bar{P}^{sc}(\theta^{inc}, \phi^{inc}, \theta^{sc}, \phi^{sc}) - \bar{P}_{meas}^{sc}(\theta^{inc}, \phi^{inc}, \theta^{sc}, \phi^{sc}))^*.$$

According to (7), in order to make a decreasing cost function with negative derivative with respect to the evolving time, the deformation velocity $F(\cdot)$ is chosen as [35]:

$$F(\bar{r}) = -\alpha \text{Re} \left[-j \sum_{i=1}^{N^{inc}} \sum_{m=1}^{N_i^{meas}} \nabla^+ \cdot (\bar{H}(\bar{r}) \times \bar{E}'(\bar{r})) \right] \quad (8a)$$

where α represents a positive normalization factor which does not affect the inversion algorithm. According to the Courant-Friedrichs-Lewy condition (CFL), the chosen time-step is inversely proportional to the maximum value of the deformation velocity [35]. Also, the update of the level set function at each pixel in the computational domain is not affected by the value of α . The electric and magnetic fields in (8a) are calculated using their limits approaching the surface from the outside as: $(\bar{r} \rightarrow S^+)$. The term $\nabla^+ \cdot (\bar{H}(\bar{r}) \times \bar{E}'(\bar{r}))$ in (8a) is calculated as follows:

$$\nabla^+ \cdot (\bar{H} \times \bar{E}') = \bar{E}' \cdot \nabla \times \bar{H} - \bar{H} \cdot \nabla \times \bar{E}' = j\omega\epsilon_0 \bar{E} \cdot \bar{E}' + j\omega\mu_0 \bar{H} \cdot \bar{H}' \quad (8b)$$

Assume that \hat{n} denotes the normal unit vector to the objects' surfaces. Upon using the boundary conditions, $\hat{n} \times E|_{S^+} = 0$ and $\hat{n} \cdot \bar{E}|_{S^+} = \frac{\nabla_s \cdot \bar{J}}{-j\omega\epsilon_0}$, $\hat{n} \times H|_{S^+} = \bar{J}$ and $\hat{n} \cdot \bar{H}|_{S^+} = 0$ where S^+ indicates approaching the surfaces from the outside, (8a) can be rewritten as [24]:

$$F(\bar{r}) = -\alpha \text{Re} \left[\sum_{i=1}^{N^{inc}} \sum_{m=1}^{N_i^{meas}} \left(\omega\mu_0 \bar{J} \cdot \bar{J}' - \frac{(\nabla_s \cdot \bar{J})(\nabla_s \cdot \bar{J}')}{\omega\epsilon_0} \right) \right] \quad (9)$$

As known in using the MoM, the surface currents densities \bar{J} and \bar{J}' will be calculated upon solving a linear system of equations $ZI = b$, where Z is the impedance matrix that involves all interactions between the patches on the object's surface at any frequency, I represents the unknown coefficients of the surface current densities, and b represents the fields on the surface due to the incident waves [29]. Since the current densities are required to be calculated for any combination of the incident and scattering directions, it is more efficient from the computational time point of view, to first invert the impedance matrix Z and then multiply it by the incident vector b that includes all different incident directions. Note that the deformation velocity is calculated at the center of patches in the triangular mesh generated by the marching cubes algorithm. For solving the Hamilton-Jacobi Equation (2), the deformation velocity needs to be extended to all pixels in the computational domain. The deformation velocity at each pixel in the domain is chosen to be the same as the velocity at the

nearest patch center on the evolving surface. The time consumed for extending the deformation velocity is about 2 minutes for a grid of $100 \times 100 \times 100$ pixels. To reduce the time, fast marching method could be used for faster extension of the deformation velocity [33].

2.3. The Marching Cubes Method

The level set method does not require any information about the surface connectivity. However the MoM forward solver is based on the surface triangular discretization of the evolving objects. Therefore, a computer graphic technique known as the *marching cubes method* is implemented to extract the triangular mesh from the 3D zero level scalar function [36, 37]. It is considered the 3D extension of the marching squares method [36].

The marching cubes method is basically a divide and conquers method. It was proposed by Lorensen and Cline [36]. The idea is based on dividing the computational domain into cubes and determining how the zero level surface intersects these cubes. At each time, eight neighbor pixels are taken to form a cube, and then the algorithm determines the triangle(s) needed to represent the part of the surface passing through this cube [36]. For each cube, an 8-bit index representing 256 possible configurations is assigned and stored. If the value of the level set function $\Phi(x_i, y_j, z_k)$ at arbitrary pixel of the cube is less than a threshold (e.g., zero) it indicates that this pixel is inside the surface and a bit value is set to one. Otherwise that pixel is located outside the evolving surface and a bit value is set to zero. The final binary value of a cube looked up in an existing table in order to determine the corresponding configuration. The triangular mesh intersects any edge of the cube with one point inside and the other one outside the surface [36].

The 256 possible configurations (corresponding to the 8-bit index of the cube) could be reduced to 15 unique configurations using reflections and symmetrical rotations [36]. In Figure 1(b), the part of a generated triangular mesh using 4 cubes, as an example, is demonstrated. The pixels P_8 , P_9 and P_{15} marked with the blue circles are located inside the evolving surface where the level set function is negative at these pixels. In order to ensure the topological consistency of the produced mesh, we have employed the version of the marching cubes method proposed by Nielson and Huang [37], which uses only the rotational properties of the cubes, that reduces the lookup table to 23 unique cases. The original marching square method may cause the generation of holes on the surface of the evolving objects [37]. A Laplacian smoothing scheme is employed here in order to improve the quality of the generated mesh, using the marching cubes method,

without modifying the mesh topology. The Laplacian scheme relocates the vertex position (x, y, z) , at its average nodes [38].

$$(x, y, z) = \frac{1}{N^{adj}} \left(\sum_{i=1}^{N^{adj}} \left(x_i^{adj}, y_i^{adj}, z_i^{adj} \right) \right) \quad (10)$$

The symbol N^{adj} represents the number of adjacent vertices to the vertex (x, y, z) , including the same vertex. The symbol $(x_i^{adj}, y_i^{adj}, z_i^{adj})$ represents the coordinates of the adjacent vertices.

In the actual implementation of the marching cubes algorithm, the resolution of the computational domain is chosen to be $100 \times 100 \times 100$ pixels. The dimensions of each cube, used in marching cubes algorithm, are five or six times larger than that of the pixel size. As the frequency hops to a higher one, the size of the cubes decreases to maintain the accuracy of the MoM-based solver.

2.4. The Level Set Algorithm

The proposed 3D level set algorithm is summarized as follows:

1. Initialize the level set function to the signed distance function. In this work, the initial guess is chosen to be a sphere (3).
2. Generate the triangular mesh representing the evolving surface using the marching cubes method.
3. Calculate the deformation velocity $F(\cdot)$ using (9) and the cost function using (4).
4. Extend the deformation velocity to the entire computational domain.
5. Update the Hamilton-Jacobi Equation (2) after a certain number of iterations (10 iterations in this work). The 10 iterations scheme is empirical. We tested many other values and observed that if less number of iterations was used, the computational time of the algorithm was larger with no considerable improvement in the final results. On the other hand, when larger number of iterations was used, the reconstruction results were not good in some cases.
6. Go to step 2 and repeat till convergence occurs.

The reconstruction algorithm is implemented using the FORTRAN programming language.

2.5. Frequency Hopping:

In most inverse scattering techniques, calculating the scattered field at single frequency does not provide enough information for retrieving

the details of the unknown target [39]. Similar to previous works of the 2D level set algorithm [25–27], the frequency hopping scheme is employed here to avoid trapping the algorithm in local minima. In this work, instead of using fixed pre-assigned number of iterations at each frequency, the stagnancy of the cost function at a working frequency is considered as the criteria for hopping to a higher frequency. This criterion avoids the unnecessary increase in the computational time when the cost function drops in local minima.

The hopping criterion is based on the most recent 20 samples calculated for the cost function. If the difference between the averages of each five successive points is less than a threshold (e.g., 1% in this work), the working frequency hops to a higher value. Let c_1 represent the average of the cost function at 5 successive iterations, c_2 represent the average of the cost function at the following 5 successive iterations, etc. Once the condition $\frac{|c_i - c_j|}{(c_i + c_j)/2} < 0.01$ for $i, j = 1, 2, 3,$ and 4 and $i \neq j$ then the working frequency hops to a higher one. This average adaptive hopping criterion was necessary due to the observed oscillations in the cost function.

2.6. The MoM Forward Solver:

In this section, the accuracy of the forward solver is validated using FEKO (3D EM simulator) [31]. The forward solver is tested to calculate the scattered fields from two PEC objects; a sphere with radius of 5 cm, centered at origin, and a cylinder with radius of 10 cm and height of 20 cm, centered at (30 cm, 0, 0). The total number of

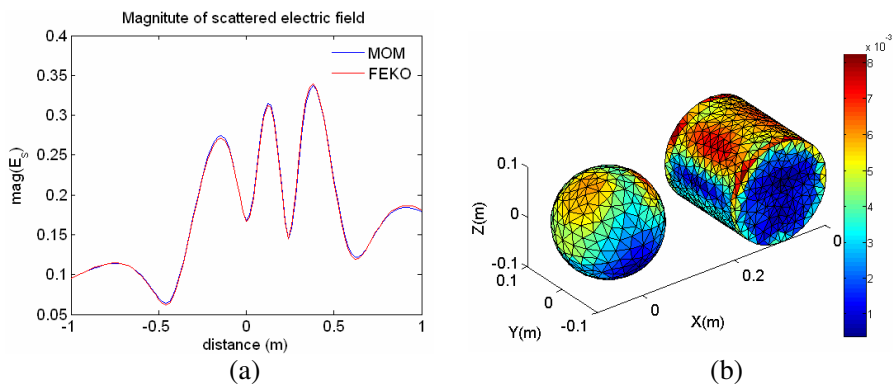


Figure 2. (a) Scattered fields and (b) the induced currents by a sphere and PEC cylinder.

triangular meshes used to represent the surface of the objects was 2212 triangles. In incident wave at 2 GHz was used to illuminate the targets, propagating in the $+z$ direction. The scattered fields are calculated at $-1 \text{ m} < x < 1 \text{ m}$, $y = 0$ and $z = 0.5 \text{ m}$. In Figure 2, the scattered fields and the induced currents on the surface of the objects using our MoM forward solver are compared with those obtained using FEKO. The results show a maximum error of 4.3% between our result and FEKO results.

It should be noted that in all results in this work the mesh used to generate the synthetic data is much denser than that used in the reconstruction algorithm.

3. NUMERICAL RESULTS

3.1. Reconstruction of a Torus:

In the first example, the reconstruction of a PEC torus is investigated. Twenty six incident plane waves with theta polarization are used to illuminate the target and 26 scattering directions per incidence are used in the reconstruction algorithm (26×26 or 676 data). The incident and scattering directions are uniformly distributed around the targets with angular steps $\Delta\theta = \Delta\phi = \pi/4$, with $0 \leq \theta \leq \pi$ and $0 \leq \phi \leq 2\pi$, as schematically shown in Figure 3(e). The 26 transmitter/receiver (T/R) directions are counted as three sets at $\theta = \pi/4, \pi/2$, and $3\pi/4$, each for eight azimuth angles $\phi = 0, \pi/4, \pi/2, 3\pi/4, \dots, 7\pi/4$, in addition to two sets at $\theta = 0$ and $\theta = \pi$. Four frequencies of $f_1 = 200 \text{ MHz}$, $f_2 = 500 \text{ MHz}$, $f_3 = 1 \text{ GHz}$ and $f_4 = 2 \text{ GHz}$ are employed in this case. The size of the computational domain is a cube of dimension 80 cm in all results presented in this work.

The initial guess is chosen here to be a sphere of radius 10 cm centered at $(x, y, z) = (30 \text{ cm}, 0, 0)$. The radius of the torus (the distance between the torus center and the tube center) is 7 cm and the tube radius is 2 cm (marked as Target in Figure 3). The torus is centered at the origin with its main plane parallel to the x - z plane. In this case, the maximum number of the inversion iterations was 7500. The resolution of the computational domain is chosen to be $100 \times 100 \times 100$ pixels. The reconstruction results at different iterations are shown in Figures 3(a)–(d). The blue transparent mesh shows the evolving surfaces while the solid red object shows the true one.

The results of Figure 3 show that the shape of torus starts to be identified after about 5000 iterations (see Figure 3(c)). The final reconstruction result is achieved after 7500 iterations which reasonably agree with the torus (Figure 3(d)).

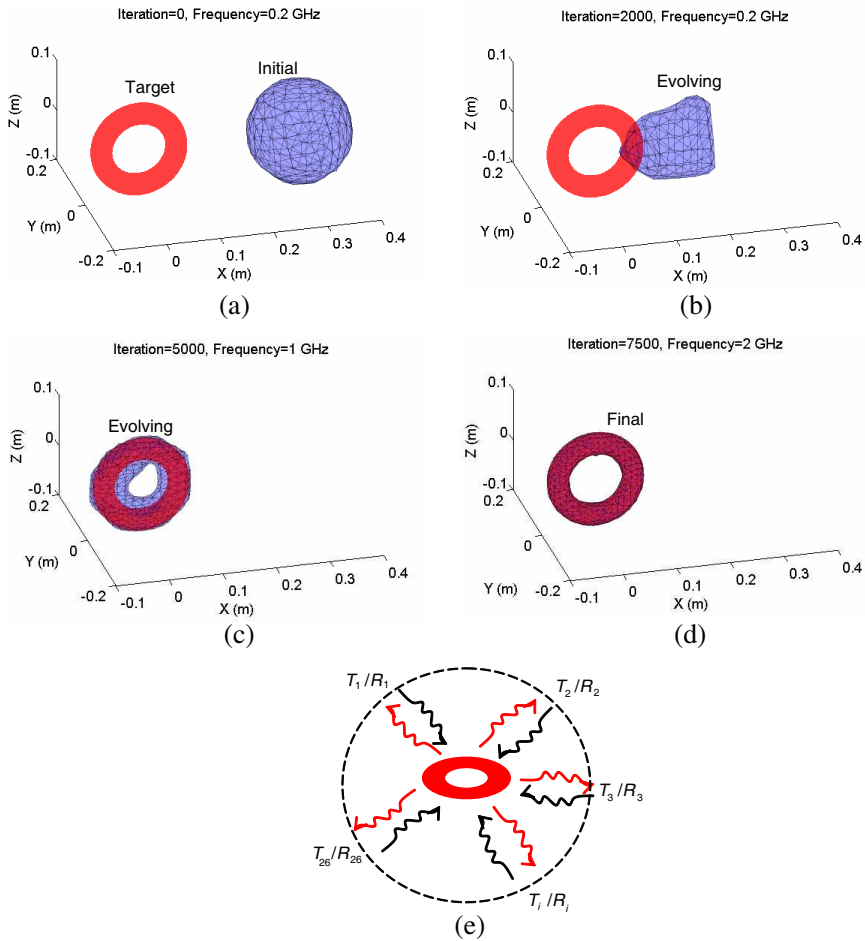


Figure 3. Reconstruction of a torus at different, (a) initial guess, (b) after 2000 iterations at 0.2 GHz, (c) after 5000 iterations at 1 GHz, (d) after 7500 iterations at 2 GHz, (e) schematic of the complete view configuration used in this example, where $i = 1, 2, \dots, 26$; T represents a transmitter or an incident direction and R represents a receiver or a scatter direction.

In addition to calculating the cost function, the surface area of the reconstructed profile at the final iteration is calculated to be $A = 551.6 \text{ cm}^2$ which shows only 0.2% error compared with the surface area of the true torus. Note that the shape has evolved from a solid sphere, initially was far from the torus, which demonstrates the capability of the level set algorithm in retrieving both location and the

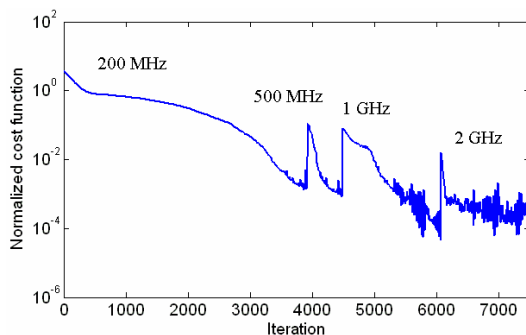


Figure 4. Normalized cost function for reconstruction of a torus.

shape of the target.

In Figure 4, the normalized cost function of the torus is plotted versus the number of iterations using a logarithmic scale. The first frequency (200 MHz) is used to retrieve the location of the torus while higher frequencies are used to retrieve the finer details of the torus. As shown in Figure 4, the working frequency hops at the following iterations: 3920, 4490, and 6080.

Fluctuations in the cost function are observed at higher frequencies (1 GHz and 2 GHz) but with negligible effect on the final reconstruction. These oscillations can be reduced upon decreasing the time step to update the Hamilton-Jacobi Equation (2), and also upon using a finer mesh for solving the forward scattering problem, with an anticipated increase in the CPU time.

The reconstruction algorithm is executed using 8 processors on Arkansas High Performance Computing Center. The details of the parallelization technique were given in [40]. The parallelized code, employs the standard message passing (MPI) for the inter-processor communications. All results presented in this work used the MPI parallelization only in the impedance matrix Z inversion part, which is the main computational bottleneck in the algorithm. In order to decrease the oscillations in the cost function in Figure 4, smaller the time steps are selected in solving (2) and also finer mesh discretization is used to solve the forward problem. This has led to an increase in the CPU time to be ~ 17 hours.

The Star of Arkansas supercomputer has 157 computing nodes, each node has quad-core Xeon E5430 processors, 2×6 MB cache, 2.66 GHz, 1333 FSB. In total, there are 1256 cores and each core has 2 GB of memory. The theoretical peak performance of Star is 13.36 Tflops.

3.2. Reconstruction of the Two Objects

In the second example, the reconstruction algorithm is examined to simultaneously retrieve PEC cylinder and cube using a single initial sphere. The cylinder has a radius of 5 cm and a height of 8 cm (marked as T_1 in Figure 5) with a center at (20 cm, 0, 0). The cube has 8 cm dimension and is centered at (0, 0, 20 cm) (marked as T_2 in Figure 5). The initial guess sphere of radius 10 cm is centered at origin. The hopping frequencies and the incident and scattering directions are the same as those used in the previous example. Notice that the volume of the cylinder is $V_1 = \pi \times 5^2 \times 8 \approx 628.3 \text{ cm}^3$. while the volume of

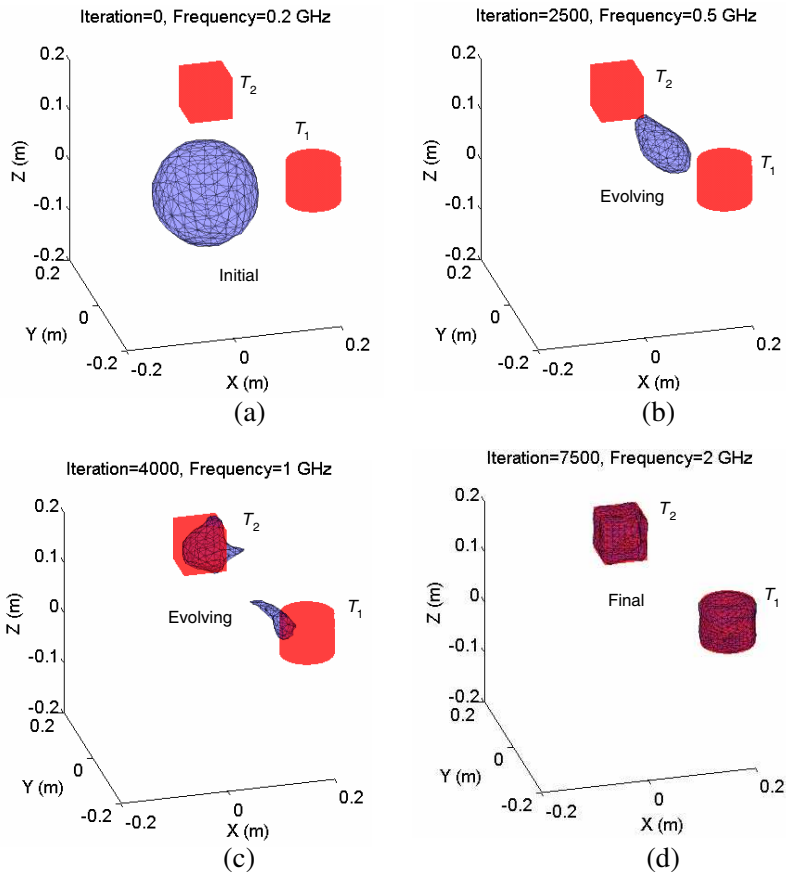


Figure 5. The reconstruction of a cylinder and a cube at different stages, (a) initial guess, (b) after 2500 iterations at 0.5 GHz, (c) after 4000 iterations at 1 GHz, (d) after 7500 iterations at 2 GHz.

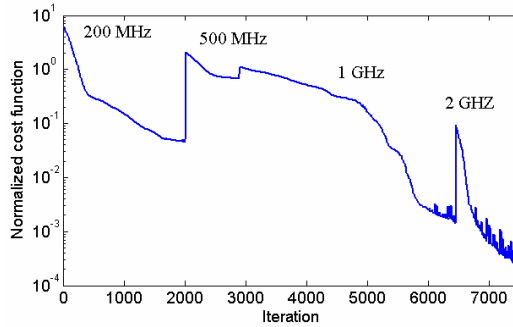


Figure 6. Normalized cost function for reconstruction of the cylinder and cube.

the cube is $V_2 = 8^3 = 512 \text{ cm}^3$, i.e., the ratio between their volumes is 1.22.

After about 4000 iterations, two separated objects start to appear (Figure 5(c)). The final reconstruction result is achieved after 7500 iterations showing a reasonable agreement with the true two objects (Figure 5(d)). The total surface area of the reconstructed profile at the final iteration is $A = 772.9 \text{ cm}^2$ which shows 2.5% error compared with the total surface area of the true objects. The normalized cost function is shown in Figure 6. The working frequency hops at the following iterations: 2020, 2910 and 6460. The reconstruction time for this case was about ~ 20 hours.

3.3. Reconstruction of Four Objects

In this example, a more complex scenario is investigated for simultaneous reconstruction of four PEC targets using a single initial guess sphere. The four objects include a sphere, an ellipsoid, a cone and a cube. The sphere of radius 4 cm is centered at (5 cm, 5 cm, -5 cm), marked as T_1 in Figure 7. The ellipsoid, centered at (-5 cm, -5 cm, -5 cm), has the equatorial radii along the y and z axes as $a = b = 3$ cm and the polar radius along the x -axis as $c = 6$ cm, marked as T_2 in Figure 7. The cone base is centered at (5 cm, 5 cm, 5 cm). The radius and the height of the cone are 4 cm and 6 cm, respectively, marked as T_3 in Figure 7. The cube with the dimension 5 cm is centered at (-5 cm, -5 cm, 5 cm), marked as T_4 in Figure 7. The initial guess sphere has radius 10 cm and is centered at origin. In this example three frequencies of $f_1 = 1.5 \text{ GHz}$, $f_2 = 2 \text{ GHz}$, $f_3 = 2.5 \text{ GHz}$ are used.

The final result at Figure 7(d) demonstrates the capability of the algorithm in handling topological changes. The total surface area of

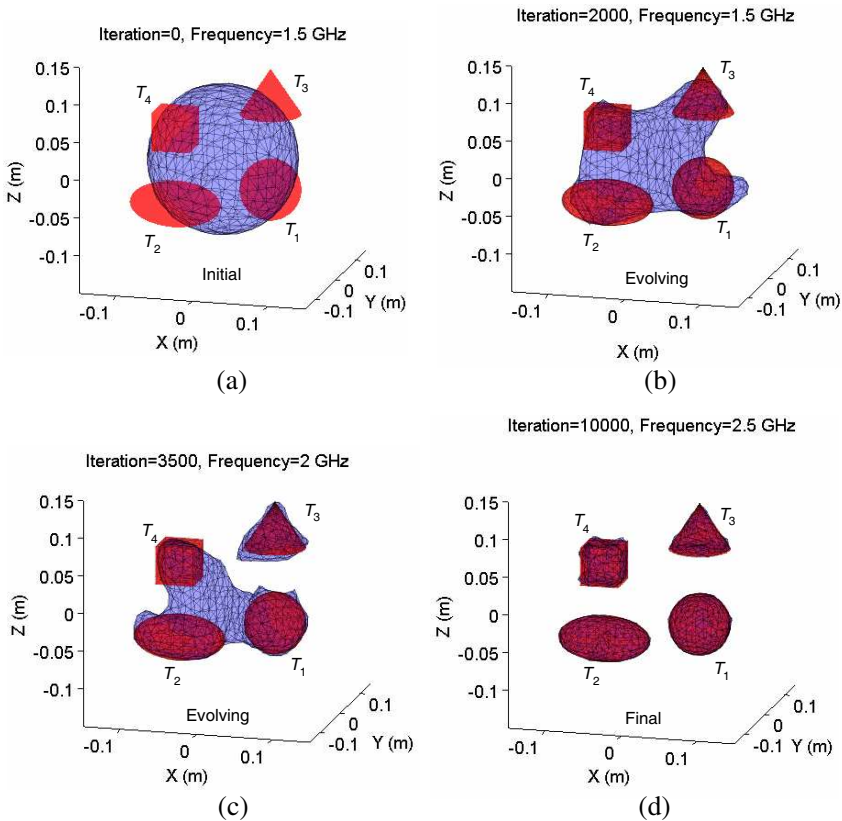


Figure 7. Reconstruction of four objects at different stages, (a) initial guess, (b) after 2000 iterations at 1.5 GHz, (c) after 3500 iterations at 2 GHz, (d) after 10000 iterations at 2.5 GHz.

the reconstructed objects is $A = 672.4 \text{ cm}^2$ which shows 1.9% error compared with the total area of the actual targets. The reconstruction time for this case was about 24 hours in this case.

The normalized cost function, in logarithmic scale, is shown in Figure 8. The working frequency hops after 2610 and 7600 iterations. In this example, due to the complexity of the examined case and the location of the initial guess sphere, different frequencies are used in the reconstruction algorithm. It should be noted that the same frequencies of the previous examples did not produce satisfactory results. Therefore we have used higher frequencies with smaller steps (500 MHz) in this case. The choice of working frequencies is currently empirical and it needs more investigation. The working frequencies are

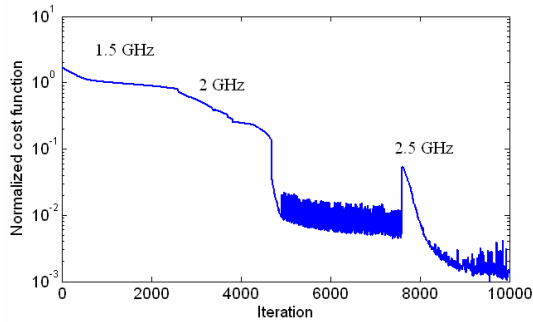


Figure 8. Normalized cost function for reconstruction of four objects.

chosen according to the complexity of the targets. If the cost function does not show convergence, more number of frequencies with smaller steps should be employed.

3.4. Reconstruction Using Limited View and Noisy Data

One of the advantages of the level set technique compared with qualitative methods, e.g., the linear sampling method, is providing good reconstruction results when using fewer number of incident and measurement directions. In practical applications, a complete multi-view measurement configuration could be difficult to be available.

Therefore the first example of the torus is revisited using a limited view of the incident and scattering directions as schematically shown in Figures 9(c) and 9(d), instead of using a complete multi-view measurement configuration shown in Figure 3(e). Two cases for the are examined; in the first case there are nine incident waves and nine measurement directions per incidence (9×9 or 81 data) following the scheme $0 \leq \theta \leq \pi/4$ and $0 \leq \phi \leq 2\pi$ with angular steps $\Delta\theta = \Delta\phi = \pi/4$. In this case, there are eight transmitter/receiver (T/R) directions at $\theta = \pi/4$ for eight azimuth angles $\phi = 0, \pi/4, \pi/2, 3\pi/4, \dots, 7\pi/4$, in addition to one set at $\theta = 0$ (see Figure 9(c)). The second case there are 17 incident waves and 17 measurement directions per incidence (17×17) or 289 data, following the scheme $0 \leq \theta \leq \pi/2$ and $0 \leq \phi \leq 2\pi$ with step of $\Delta\theta = \Delta\phi = \pi/4$. In this case, there are 16 transmitter/receiver directions at $\theta = \pi/4$ and $\pi/2$, each for eight azimuth angles $\phi = 0, \pi/4, \pi/2, 3\pi/4, \dots, 7\pi/4$, in addition to one set at $\theta = 0$ (see Figure 9(d)). The reconstruction results for both cases are shown in Figures 9(a) and 9(b), respectively.

Notice that in the 26×26 configuration case, the incident and scattering directions are placed uniformly all around the targets as

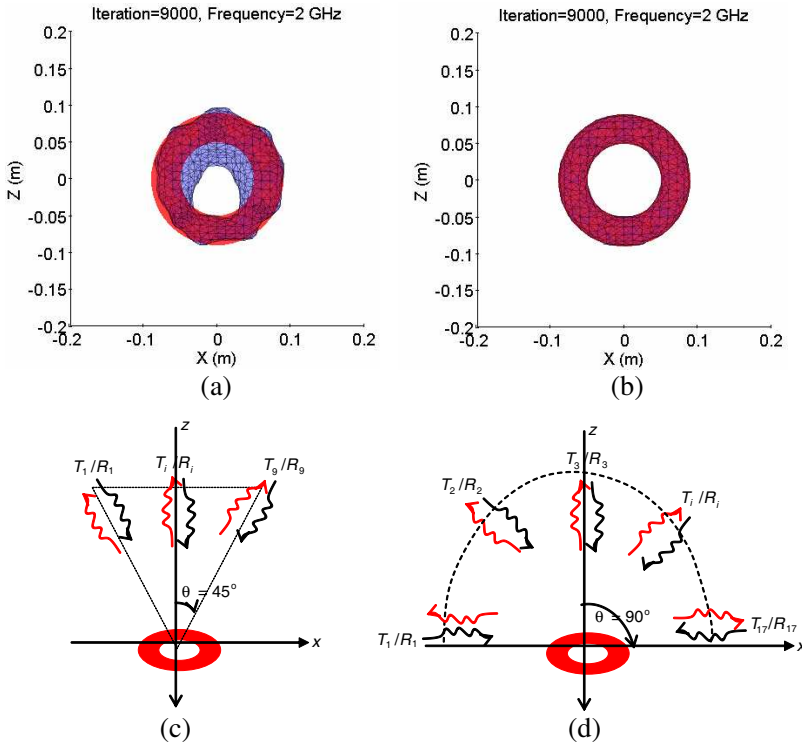


Figure 9. Reconstruction of the torus using limited view data (a) 81 data (9×9) per frequency, (b) 289 data (17×17) per frequency, (c) limited view sketch for Figure 9(a) where the incident and scatter directions (T/R sets) are located as shown with $i = 1, 2, \dots, 9$, $0 \leq \theta \leq \pi/4$ and $0 \leq \phi \leq 2\pi$ and (d) limited view sketch for Figure 9(b) where the incident and scatter directions (T/R sets) are located as shown with $i = 1, 2, \dots, 17$, $0 \leq \theta \leq \pi/2$ and $0 \leq \phi \leq 2\pi$.

sketched in Figure 3(e), which is not the case in the limited view 17×17 configuration of Figures 9(d)–(c).

The final reconstructed result in Figure 9(a) is observed to be larger than the actual torus. However the result of Figure 9(b) demonstrates very good reconstruction of the true torus, even when there is no illumination from one side of the object. The errors in the reconstructed surface areas are 12.2% in the 9×9 data case (Figure 9(c)) and 0.008% in the 17×17 data case (Figure 9(d)).

In addition, the performance of the reconstruction algorithm using noisy input data corresponding to two different levels of signal to noise

ratio (SNR) is investigated. The SNR is defined as:

$$\text{SNR} = 20 \log \left(\frac{E_{\text{signal}}^{\text{rms}}}{E_{\text{noise}}^{\text{rms}}} \right) \quad (11)$$

where $E_{\text{signal}}^{\text{rms}}$ and $E_{\text{noise}}^{\text{rms}}$ represent the root-mean-square of the signal and the noise, respectively. The same number of incident and measurement directions is used in this example similar to the 26×26 case in Figure 3. Two levels of noise in input data are examined here corresponding to SNR = 10 dB and 5 dB, and the final reconstruction results are shown in Figures 10(a) and 10(b), respectively. The results show that the level set algorithm provided reasonable reconstruction accuracy even with SNR = 5 dB. The errors in surface areas are 36% when SNR = 5 dB (Figure 10(a)) and 12.6% when the SNR = 10 dB (Figure 10(b)).

The reconstruction errors in the surface areas and cost functions are summarized in Table 1. The error in the reconstructed surface area using *noiseless* complete view data was observed to be $\sim 2.5\%$ for the case of the cylinder and the cube. The error was observed to be $\sim 0.2\%$ for the torus case when using noiseless data and complete view data. An increased error of $\sim 36\%$ was observed when SNR = 5 dB noisy data even with using complete view data; however the general shape of the torus is reconstructed and can be reasonably identified. In all cases, the errors in the cost function were small except when the SNR = 5 dB or even 10 dB, as anticipated.

Table 1. The surface areas errors in the reconstructed shapes.

Case	Surface area of the reconstructed object (cm ²)	Surface area of the true object (cm ²)	Error in surface area (%)	Error in cost function (%)
Torus	551.6	552.7	0.2	0.0121
Two objects	772.9	792.4	2.5	0.0544
Four objects	672.4	685.3	1.9	0.1353
Torus (81 data)	620	552.7	12.2	0.5726
Torus (289 data)	552.6	552.7	0.008	0.013
Torus (SNR = 5 dB)	752.3	552.7	36	65.7
Torus (SNR = 10 dB)	622.5	552.7	12.6	35.6

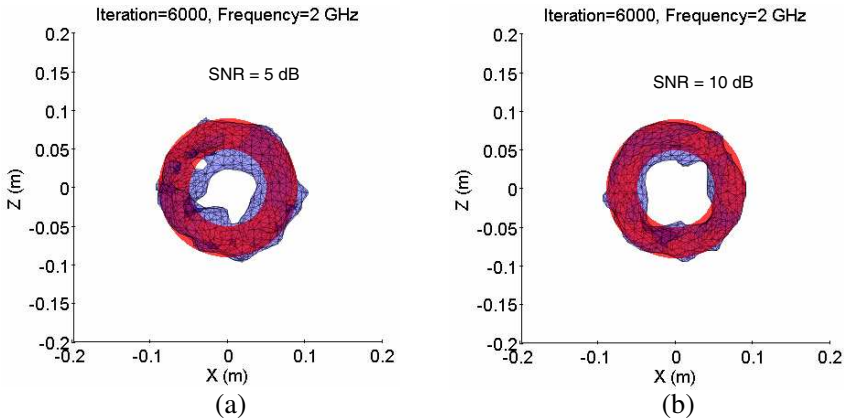


Figure 10. Reconstruction of the torus using noisy data. (a) SNR = 5 dB. (b) SNR = 10 dB using the same data of Figure 3.

4. CONCLUSIONS

In this work, a three-dimensional level set technique was implemented for retrieving the shape and the location of 3D PEC targets immersed in air. The surface integral equation was used as the forward solver providing relatively fast reconstruction of the unknown objects, compared with volume integral equation methods. The marching cube algorithm was implemented to generate the surface triangular meshes needed for the MoM solver during the inversion process. This algorithm required negligible time to generate the triangular meshes when compared with other parts of the inversion algorithm, mainly the calculations of the impedance matrix and its inversion needed to calculate the deformation velocity.

Employing the level set framework provided simultaneous reconstruction of multiple objects using single initial guess. The algorithm was designed such that the working frequency hops to a higher value when the cost function stagnated in local minima. In addition to demonstrating the cost function as a quantitative metric, the surface areas of the reconstructed objects were calculated. For practical situations, the level set algorithm demonstrated satisfactory capability when limited view data was examined, which is not the case in other techniques such as the linear sampling method, for example. Another realistic consideration was the demonstration of reasonable reconstruction results when using noisy data of SNR = 10 dB and 5 dB. As anticipated, the SNR = 10 dB case provided better results compared with the 5 dB case. The MPI parallel programming was

employed here to achieve reduction in the required CPU time of the algorithm (details were reported in [40]).

Regardless of the shape symmetry, and based on several examples not presented here but presented in [41], the level set algorithm proved capability for reconstructing non-symmetric shapes using noisy data down to $\text{SNR} = 10$ dB. Although the synthetic data used in this work were obtained using our MoM forward solver, the accuracy of our computer code was validated with results obtained using FEKO as shown in Figure 2. Moreover, the capability of the level set algorithm was demonstrated in reconstructing 2D PEC targets using experimental data as discussed in [42] and [43].

The number of the hopping frequencies used in the algorithm is selected empirically, i.e., using numerical experiments. From our experience in shape reconstruction, the number of needed frequencies increases with the increase in shape complexity and noise level in the data. Also, lower frequencies retrieved the location of the unknown targets depending on the initial guess. In this work, the measurements data were all *synthetic*; therefore there were no constraints on the band width of the used frequency, although they were selected in the low GHz based on the size of the considered objects. Also, due to the simplicity of the shapes considered in this work, few frequencies were needed. However, in our experimental work reported in [42] and [43], the used frequency was constrained by the bandwidth of the actual antennas (Vivaldi and/or Dielectric Resonator antennas). However, the frequency step was decreased as needed to increase the number of frequencies involved in the hopping scheme.

ACKNOWLEDGMENT

This work was supported in part by the National Science Foundation under Grant MRI 0421099 (Red Diamond) and Grant MRI #072265 (Star of Arkansas).

REFERENCES

1. Zhou, H., T. Takenaka, J. Johnson, and T. Tanaka, "A breast imaging model using microwaves and a time domain three dimensional reconstruction method," *Progress In Electromagnetics Research*, Vol. 93, 57–70, 2009.
2. Caramanica, F. and G. Oliveri, "An innovative multi-source strategy for enhancing the reconstruction capabilities of inverse scattering techniques," *Progress In Electromagnetics Research*, Vol. 101, 349–374, 2010.

3. Solimene, R., A. Brancaccio, R. Di Napoli, and R. Pierri, "3D sliced tomographic inverse scattering experimental results," *Progress In Electromagnetics Research*, Vol. 105, 1–13, 2010.
4. Ramm, A. G., *Inverse Problems: Mathematical and Analytical Techniques with Applications to Engineering*, Springer, 2004.
5. Pastorino, M., "Recent inversion procedures for microwave imaging in biomedical, subsurface detection and nondestructive evaluation applications," *Imaging Measurement Systems*, Vol. 36, Nos. 3–4, 257–269, Oct.–Dec. 2004.
6. El-Shenawee, M. and E. Miller, "Spherical harmonics microwave algorithm for shape and location reconstruction of breast cancer tumor," *IEEE Transactions on Medical Imaging*, Vol. 25, No. 10, 1258–1271, Oct. 2006.
7. Huang, H., X. Qu, J. Liang, X. He, X. Chen, D. Yang, and J. Tian, "A multi-phase level set framework for source reconstruction in bioluminescence tomography," *Journal of Computational Physics*, Vol. 229, No. 13, 5246–5256, Jul. 2010.
8. Hohage, T., "Fast numerical solution of the electromagnetic medium scattering problem and applications to the inverse problem," *Journal of Computational Physics*, Vol. 214, No. 1, 224–238, May 2006.
9. Hea, L., S. Kindermann, and M. Sin, "Reconstruction of shapes and impedance functions using few far-field measurements," *Journal of Computational Physics*, Vol. 228, No. 3, 717–730, Feb. 2009.
10. Bao, G., S. Houb, and P. Li, "Inverse scattering by a continuation method with initial guesses from a direct imaging algorithm," *Journal of Computational Physics*, Vol. 227, No. 1, 755–762, Nov. 2007.
11. Travassos, X. L., D. A. G. Vieira, N. Ida, C. Vollaire, and A. Nicolas, "Inverse algorithms for the GPR assessment of concrete structures," *IEEE Transactions on Magnetics*, Vol. 44, No. 6, 994–997, Jun. 2008.
12. Soldovieri, F., A. Brancaccio, G. Prisco, G. Leone, and R. Pierri, "A Kirchhoff-based shape reconstruction algorithm for the multimonostatic configuration: The realistic case of buried pipes," *IEEE Transactions on Geoscience and Remote Sensing*, Vol. 46, No. 10, 3031–3038, Oct. 2008.
13. Brignone, M., G. Bozza, A. Randazzo, M. Piana, and M. Pastorino, "A hybrid approach to 3D microwave imaging by using linear sampling and ACO," *IEEE Trans. on Antennas and Propagation*, Vol. 56, No. 10, 3224–3232, Oct. 2008.

14. Catapano, I., L. Crocco, M. D'Urso, and T. Isernia, "3D microwave imaging via preliminary support reconstruction: Testing on the Fresnel 2008 database," *Inverse Problems*, Vol. 25, No. 2, Feb. 2009.
15. Tortel, H., "Electromagnetic imaging of a three-dimensional perfectly conducting object using a boundary integral formulation," *Inverse Problems*, Vol. 20, 385–398, 2004.
16. Catapano, I., L. Crocco, and T. Isernia, "Improved sampling methods for shape reconstruction of 3-D buried targets," *IEEE Trans. on Geoscience and Remote Sensing*, Vol. 46, No. 10, 3265–3273, Oct. 2008.
17. Yu, C., M. Yuan, and Q. H. Liu, "Reconstruction of 3D objects from multi-frequency experimental data with a fast DBIM-BCGS method," *Inverse Problems*, Vol. 25, No. 2, Feb. 2009.
18. Vouldis, A. T., C. N. Kechribaris, T. A. Maniatis, K. S. Nikita, and N. K. Uzunoglu, "Investigating the enhancement of three-dimensional diffraction tomography by using multiple illumination planes," *Journal of Optical Society of America*, Vol. 22, No. 7, 1251–1262, Jul. 2005.
19. Zaeytjij, J. D., A. Franchois, C. Eyraud, and J. M. Geffrin, "Full-wave three-dimensional microwave imaging with a regularized Gauss-Newton method — Theory and experiment," *IEEE Trans. on Antennas and Propagation*, Vol. 55, No. 11, 3279–3292, Nov. 2007.
20. Saeedfar, A. and K. Barkeshli, "Shape reconstruction of three-dimensional conducting curved plates using physical optics, nurbs modeling, and genetic algorithm," *IEEE Trans. on Antennas and Propagation*, Vol. 54, No. 9, 2497–2507, Sep. 2006.
21. Solimene, R., A. Buonanno, R. Pierri, and F. Soldovieri, "Shape reconstruction of 3D metallic objects via a physical optics distributional approach," *AEU International Journal of Electronics and Communications*, Vol. 64, No. 2, 142–151, Feb. 2010.
22. Banasiak, R. and M. Soleimani, "Shape based reconstruction of experimental data in 3D electrical capacitance tomography," *NDT & E International*, Vol. 43, No. 3, 241–249, Apr. 2010.
23. Çayören, M., I. Akduman, A. Yapa, and L. Crocco, "A new algorithm for the shape reconstruction of perfectly conducting objects," Vol. 23, No. 3, 1087–1100, Apr. 2007.
24. El-Shenawee, M., O. Dorn, and M. Moscoso, "An adjoint-field technique for shape reconstruction of 3-D penetrable object immersed in lossy medium," *IEEE Transactions on Antennas and*

- Propagation*, Vol. 57, No. 2, 520–534, Feb. 2009.
25. Ferrayé, R., J. Dauvignac, and C. Pichot, “An inverse scattering method based on contour deformations by means of a level set method using frequency hopping technique,” *IEEE Transactions On Antennas and Propagation*, Vol. 51, No. 5, May 2003.
 26. Litman, A., “Reconstruction by level sets of n-ary scattering obstacles,” *Inverse Problems*, Vol. 21, No. 6, 131–152, Dec. 2005.
 27. Van den Doel, K. and U. M. Ascher, “On level set regularization for highly ill-posed distributed parameter estimation problems,” *J. Computational Physics*, Vol. 216, No. 2, 707–723, Aug. 2006.
 28. Hajihashemi, M. R. and M. El-Shenawee, “TE versus TM for the shape reconstruction of 2-D PEC targets using the level-set algorithm,” *IEEE Transactions on Geoscience and Remote Sensing*, Vol. 48, No. 3, 1159–1168, Mar. 2010.
 29. Rao, S. M., D. R. Wilton, and A. W. Glisson, “Electromagnetic scattering by surfaces of arbitrary shape,” *IEEE Transaction on Antennas and Propagation*, Vol. 30, No. 3, 409–418, May 1982.
 30. Makarov, S. N., *Antenna and EM Modeling with Matlab*, 1st edition, Wiley Press, 2002.
 31. FEKO User’s Manual, Suite 5.3, Jul. 2007.
 32. Gibson, W. C., *The Method of Moments in Electromagnetics*, Chapman & Hall/CRC Press, 2007.
 33. Sethian, J. A., *Level Set Methods and Fast Marching Methods*, Cambridge University Press, 1999.
 34. Osher, S. J. and R. P. Fedkiw, *Level Set Methods and Dynamic Implicit Surfaces*, Springer-Verlag, 2003.
 35. Roger, A., “Reciprocity theorem applied to the computation of functional derivatives of the scattering matrix,” *Electro-Magnetics*, Vol. 2, No. 1, 69–83, 1982.
 36. Lorensen, W. E. and H. E. Cline, “Marching cubes: A high resolution 3D surface construction algorithm,” *Computer Graphics*, Vol. 21, No. 4, Jul. 1987.
 37. Nielson, G. M. and A. Huang, “Approximating normals for marching cubes applied to locally supported isosurfaces,” *IEEE Visualization Proceedings*, 459–466, Oct. 2002.
 38. Hansen, G. A., R. W. Douglass, and A. Zardecki, *Mesh Enhancement*, Imperial College Press, 404, 2005.
 39. Chew, W. C. and J. H. Lin, “A frequency-hopping approach for microwave imaging of large inhomogenous bodies,” *IEEE Microwave and Wave Guided Letters*, Vol. 5, No. 12, 439, Dec. 1995.

40. Hajihashemi, M. R. and M. El-Shenawee, "High performance computing for the level-set reconstruction algorithm," *J. of Parallel and Distributed Computing*, Vol. 70, No. 6, 671–679, Jun. 2010.
41. Hajihashemi, M. R., "Inverse scattering level set algorithm for retrieving the shape and location of multiple targets," Ph.D. Dissertation, University of Arkansas, 2010.
42. Hassan, A., M. Hajihashemi, M. El-Shenawee, A. Al-Zoubi, and A. Kishk, "Drift De-noising of experimental TE measurements for imaging of 2D PEC cylinder using the level set algorithm," *IEEE Antennas and Wireless Propag. Letters*, Vol. 8, 1218–1222, 2009.
43. Woten, D. A., M. R. Hajihashemi, A. M. Hassan, and M. El-Shenawee, "Experimental microwave validation of the level-set reconstruction algorithm," *IEEE Transaction on Antennas and Propagation*, Vol. 58, No. 1, 230–233, Jan. 2010.